ACS Catalysis

Research Article

pubs.acs.org/acscatalysis

Rapid Microwave-Assisted Polyol Reduction for the Preparation of Highly Active PtNi/CNT Electrocatalysts for Methanol Oxidation

Abu Bakr Ahmed Amine Nassr,[†,∥] Ilya Sinev,[‡] Marga-Martina Pohl,[§] Wolfgang Grünert,[‡] and Michael Bron*[,†]

[†]Department of Chemistry, Faculty of Natural Science II, Martin-Luther-University Halle-Wittenberg, von-Danckelmann-Platz 4, 06120 Halle (Saale), Germany

[‡]Laboratory of Industrial Chemistry, Faculty of Chemistry and Biochemistry, Ruhr-University Bochum, Universitätsstraße 150, 44780 Bochum, Germany

[§]Leibniz-Institut für Katalyse e.V. an der Universität Rostock (LIKAT), Albert-Einstein-Straße 29a, 18059 Rostock, Germany

Supporting Information

ABSTRACT: PtNi nanoparticle catalysts supported on oxygen functionalized carbon nanotubes were prepared by microwave-assisted polyol reduction using two different modes of irradiation, namely, continuous or pulsed irradiation. The influence of irradiation time or pulse number on catalyst structure and activity in methanol electrooxidation has been studied. Characterization was done with ICP-OES, XRD, TEM, XPS, and XAS to determine composition, morphology, crystal structural and chemical state. The electrocatalytic activity has been evaluated by cyclic voltammetry (CV) and chronoamperometry (CA). PtNi nanoparticles are present in alloy form and are well dispersed on the carbon nanotubes. Pt is in its metallic state, whereas Ni is present in metallic and oxidized form depending on the preparation conditions. The electrocatalytic activity both in terms of surface and mass specific activity is higher than that of the state-of-the-art-catalyst Pt/C (E-TEK). The enhancement of the electrocatalytic activity is discussed with respect to PtNi alloy formation and the resulting modification of the electronic properties of Pt by Ni in the alloy structure. The microwave assisted polyol method with continuous irradiation is more effective in the preparation of PtNi electrocatalysts both in terms of reaction time and activity than the pulsed microwave method.

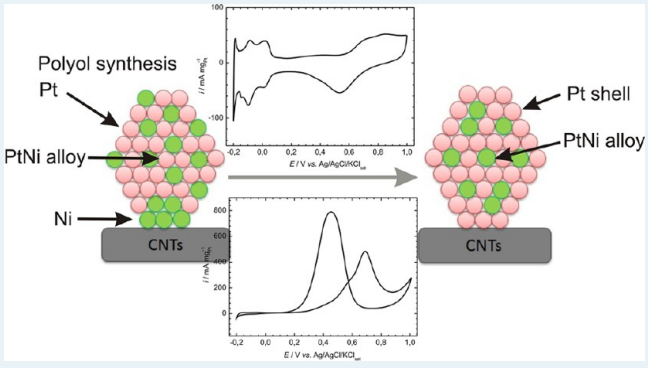

KEYWORDS: *microwave irradiation, polyol method, platinum, nickel, methanol electrooxidation, direct methanol fuel cell*

1. INTRODUCTION

Methanol has received significant attention as fuel in low temperature fuel cells (DMFCs, direct methanol fuel cells), which are discussed as possible power sources for many portable and transportation applications ranging from mobile phones to vehicles.[1,2] Methanol has several advantages compared to hydrogen: it is easy and safe to handle, store, and transport. Furthermore, it has a higher energy density than hydrogen and can be produced from biomass via syngas or through fermentation of agricultural products.[3−6] However, the electrooxidation of methanol occurring on the anode side of DMFCs is associated with poor kinetics and a resulting decrease in cell efficiency. The development of highly active anode catalysts is urgently needed to overcome these technical obstacles.

Pt is well-known as the most active catalytic material for methanol oxidation but surface poisoning with CO molecules formed as an intermediate during methanol oxidation quickly deteriorates the activity of Pt electrodes when used as a catalyst in direct methanol fuel cells.[7] It is well-established that complete methanol oxidation is a complex multistep reaction that requires active sites for methanol adsorption and dehydrogenation as well as sites for supplying oxygen-containing species for the oxidation of the carbonaceous intermediates formed during adsorption and dehydrogenation.[8−11]

The methanol oxidation on Pt can be represented by three main steps. The first two steps involve the adsorption of methanol and its dehydrogenation to form adsorbed CO. In the third step, the adsorbed CO is oxidized with the aid of oxygen-containing species (e.g., −OH) formed on the Pt surface. The mechanism can be written by the following eqs 1−3.[11]

$$CH_3OH + Pt \rightarrow Pt{-}(CH_3OH)_{ads} \quad (1)$$

$$Pt{-}(CH_3OH)_{ads} \rightarrow Pt{-}(CO)_{ads} + 4H^+ + 4e^- \quad (2)$$

Received: December 3, 2013
Revised: June 12, 2014
Published: June 13, 2014

$$Pt{-}(CO)_{ads} + H_2O \rightarrow Pt + CO_2 + 2H^+ + 2e^- \quad (3)$$

Indeed, the fact that oxygen-containing species form on the Pt surface only at higher potentials (>0.7 V vs RHE) creates a significant overpotential that limits the applicability of Pt catalysts for the methanol oxidation reaction (MOR).[8,11]

Alloying of Pt with a second metal that can supply the oxygen species at lower potentials is one strategy to decrease the poisoning of the Pt surface with CO and enhance the activity of the catalyst toward methanol oxidation.[12−14] Second metals such as M = Ru, Sn, Au, Co, Ni, or Pd[13−18] have been suggested. Moreover, transition metal oxides have also been demonstrated to serve the same purpose.[19−24] The mechanism can then be represented by the following eqs 4, 5, and 6:

$$Pt{-}(CH_3OH)_{ads} \rightarrow Pt{-}(CO)_{ads} + 4H^+ + 4e^- \quad (4)$$

$$M + H_2O \rightarrow M{-}OH_{ads} + H^+ + e^- \quad (5)$$

$$Pt{-}(CO)_{ads} + M{-}OH_{ads} \rightarrow Pt + M + CO_2 + H^+ + e^- \quad (6)$$

Besides this so-called bifunctional mechanism, the electronic mechanism or ligand effect has also been postulated.[25,26] It is assumed that the second metal can modify the electronic properties of Pt by changing the electron density of states of the d-band and the Fermi level energy. This electronic modification destabilizes the interaction between the CO molecules and the Pt surface and hence weakens the Pt−CO bonding.[17,26,27]

PtNi catalysts exhibit good catalytic activity for methanol oxidation and are considered more economical than other systems owing to the lower cost of Ni.[17,27−29] The electronic mechanism of Ni in Ni containing catalysts (PtNi and PtRuNi) has been confirmed experimentally.[27] Higher activity of Ni containing catalysts was explained by electron transfer from Ni to Pt detected from shifts in the Pt 4f binding energy to lower values, resulting in a weakening of the adsorption of CO molecules onto the Pt surface. Recently, a DFT study confirmed the downshift of the Pt d-band center as a result of Ni incorporation, decreasing the interaction between Pt and CO, consistent with XPS and electrochemical results.[17,26,27]

Electrocatalysis is a surface reaction that depends strongly on the surface properties of the catalyst onto which the reactants adsorb and react to give the products. Thus, the structural properties of the catalysts like particle size and shape as well as interaction with the support are important factors controlling the catalytic process. The catalyst preparation methods should be tuned to yield the desired catalyst features which lead finally to the required higher activity. Microwave synthesis is one of the recent techniques for synthesis of catalysts with nanosized particles, high dispersion, and narrow particle size distribution which meet the demanded higher catalytic activity for fuel cell applications.[28,29] The advantage of microwave preparation is the fast and homogeneous heating resulting from the interaction of microwave radiation directly with the solvent molecules and the reducing agent. Short nucleation and crystallization time can be achieved resulting in small particle sizes and high dispersion. Also, the generation of localized high temperature as a result of the fast heating enhances the rate of metal ion reduction. Moreover, the simplicity of the equipment and the short reaction time render this technique energy saving and meet economical considerations.[30,31] Despite many studies on the influence of preparation conditions on Pt and Pt-based electrocatalysts for fuel cell applications using microwave assisted synthesis,[24,28,29] there was no such study on PtNi catalysts which could show how the mode of irradiation influences their structural properties and hence offers an avenue to tune their catalytic behavior.

In this study, we report on the preparation of PtNi nanocatalysts supported on oxygen functionalized carbon nanotubes (FCNTs) using the microwave-assisted polyol method in which ethylene glycol (EG) is used as solvent and reducing agent at the same time. The effects of irradiation mode (continuous or pulsed irradiation), the irradiation duration under these two modes, as well as aging of the catalyst prepared under continuous irradiation on catalyst structure were studied with ICP-OES, XRD, TEM, XPS, and XAS. The catalytic activity of the prepared catalysts toward methanol oxidation has been evaluated and discussed in relation to the structural properties and compared with the benchmark catalyst Pt/C from E-TEK.

2. EXPERIMENTAL WORK

2.1. Catalyst Preparation. PtNi catalysts supported on functionalized carbon nanotubes (FCNTs) were prepared using microwave-assisted polyol reduction according to the following procedures. First, the as-received CNTs (Baytubes C 150 P, obtained from Bayer Material Science AG, Germany) were functionalized with 5 M HNO_3 as reported elsewhere[32] to create oxygen functional groups on the surface of CNTs. A total of 100 mg of FCNTs were dispersed under stirring in 30 mL of ethylene glycol (EG). To this dispersion, the required amounts of metal salts dissolved in EG (5 mL of 0.0197 M H_2PtCl_6 and 5 mL of 0.0197 M $Ni(NO_3)_2 \cdot 6H_2O$) were added dropwise in sequence under stirring and left under stirring for 30 min. The pH of the mixture was modified with 2 M NaOH/EG to pH 11, and the suspension was left stirring for 30 min. Then the solution was sonicated in an ultrasonic bath for 15 min. For metal ion reduction, the mixture was transferred into a microwave reactor (Microwave START 1500, Milestone) where it was irradiated at 700 W either continuously for a defined time or in a pulsed mode with a pulse duration of 20 s (10 s on and 10 s off) for a specific number of pulses. Figure S1 in the Supporting Information demonstrates the temperature profiles recorded in the reactor during these two modes of irradiation. The microwave step was followed by aging of the catalyst under stirring overnight. Two reference samples were prepared, one without aging and one with pH modification during the aging step by the addition of 250 mL of 0.1 M HNO_3. The detailed preparation conditions are summarized in Table 1. The catalysts were separated by centrifugation (Centrifuge 4807, Eppendorf) for 20 min at 5000 rpm and subjected to 5−6 washing cycles with water before drying at 80 °C overnight. Finally, the catalysts were crushed in a mortar and stored in glass vials until used. In the preparations, we aimed at a metal loading of 20 wt %. The Pt/Ni atomic ratio in the precursor solution was 1.

All catalysts are labeled PtNi/CNT followed by a "C" and the irradiation duration in seconds for continuous irradiation and a "P" and the pulse number for pulsed irradiation. For example, PtNi/CNT_C_90 and PtNi/CNT_P_18 refer to catalysts prepared with continuous irradiation for 90 s and with pulsed irradiation for 18 pulses, respectively.

2.2. Structural Catalyst Characterization. The metal loadings of both Pt and Ni on the support and their atomic ratio were determined with inductively coupled plasma−optical emission spectroscopy (ICP-OES; JOBIN YVON ULTIMA 2,

Table 1. Details of the Preparation Conditions for PtNi/CNT Catalysts under Microwave Irradiation

PtNi/CNT catalysts	irradiation mode	reaction time	aging conditions
C_90_na	continuous	90 s	separated directly after cooling
C_90_acid	continuous	90 s	stirring overnight after pH modification
C_90	continuous	90 s	stirring overnight without pH modification
C_60	continuous	60 s	stirring overnight without pH modification
C_50	continuous	50 s	stirring overnight without pH modification
C_40	continuous	40 s	stirring overnight without pH modification
P_6	pulsed	6 cycles	stirring overnight without pH modification
P_9	pulsed	9 cycles	stirring overnight without pH modification
P_12	pulsed	12 cycles	stirring overnight without pH modification
P_18	pulsed	18 cycles	stirring overnight without pH modification

HORIBA). The samples were subjected to microwave digestion in aqua regia following the procedure in ref 32. After dilution with water, the metal ion concentration was measured with ICP-OES. To ensure the validity of the method, a reference catalyst (20% Pt/C from E-TEK) was subjected to the same procedure. For conventional transmission electron microscopy (TEM) analysis, a dispersion of the catalyst sample in ethanol was prepared by sonication for 10 min and a few drops of this dispersion were dropped onto a carbon coated copper grid and investigated with a LEO 912 microscope working at an acceleration voltage of 120 keV.

HR-TEM measurements were performed at 200 kV with an aberration-corrected JEM-ARM200F (JEOL, Corrector: CEOS). The microscope is equipped with a JED-2300 (JEOL) energy-dispersive X-ray-spectrometer (EDXS) for chemical analysis. The aberration corrected STEM imaging (High-Angle Annular Dark Field (HAADF) and Annular Bright Field (ABF)) were simultaneously performed under the following conditions. HAADF and ABF both were done with a spot size of approximately 0.13 nm, a convergence angle of 30−36°, and collection semiangles for HAADF and ABF of 90−170 mrad and 11−22 mrad, respectively. Preparation of the TEM sample: The sample was suspended in heptane, deposited on a holey carbon supported Cu-grid (mesh 300), and transferred to the microscope.

The crystal structure of the prepared catalysts was identified by XRD. The data was collected with a D8 advanced X-ray diffractometer, Bruker AXS, working with a Cu Kα source (λ = 0.15406 nm) in the 2θ range of 20−90° at a scan rate of 2° min^{-1}.

X-ray photoelectron spectroscopy (XPS) measurements were carried out in an ultrahigh vacuum (UHV) setup equipped with a monochromatic Al Kα X-ray source ($h\nu$ = 1486.6 eV), operated at 14.5 kV and 35 mA, and a high resolution Gammadata-Scienta SES 2002 analyzer. The base pressure in the measurement chamber was maintained at about 7×10^{-10} bar. The measurements were carried out in the fixed transmission mode with a pass energy of 200 eV resulting in an overall energy resolution of 0.25 eV. High-resolution spectra for C 1s, O 1s, Ni 2p, and Pt 4f regions were recorded. The binding energy (BE) scales were recalibrated based on the C 1s line of the sp^2 hybridized graphitic carbon, which was set to 284.5 eV. Data reduction and signal shape analysis were performed using the program package CASA XPS. Atomic ratios of elements were calculated from intensity ratios using the Scofield photoionization cross-section data together with the analyzer work function provided by the manufacturer. The Pt peak area was determined by simple integration employing a Shirley-type background in a preselected binding energy (BE) window.

Pt L_3-edge (11564 eV) X-ray absorption fine structure spectroscopy (XAFS) measurements were carried out at the SUPERXAS beamline of the Swiss Light Source (Paul Scherrer Institute, Villigen, Switzerland). A channel-cut Si (311) monochromator was used to tune the energy of the incident beam while a Rh-coated toroid mirror was used to cut unwanted higher harmonics. The spectra were recorded in the transmission mode at ambient temperature. For the measurements, the samples were pressed into self-supporting pellets (diameter, 13 mm) and wrapped with Kapton tape. Pt L_3-edge energy calibration was done by measuring the spectrum of a Pt foil placed between the second and third ionization chambers together with the sample spectra. All spectra were measured twice to ensure their reproducibility.

Analysis of the Extended X-ray Absorption Fine Structure (EXAFS) was performed with the VIPER for Windows software.[33] In the spectra of the absorption coefficient μ, a Victorian polynomial was fitted to the pre-edge region for background subtraction. A smooth atomic background μ_0 was evaluated using a smoothing cubic spline. The Fourier analysis of the k^2- weighted experimental functions $\chi = (\mu - \mu_0)/\mu_0$ was performed with a Kaiser window. The required scattering amplitudes and phase shifts were calculated by the ab initio FEFF8.10 code[34] using the models for fcc Pt metal, orthorhombic PtO_2 and fcc Pt−Ni alloy structures. The fitting was done in the *k*- and *r*-spaces. The shell radius *r*, coordination number CN, Debye−Waller factor σ^2, and adjustable "muffin-tin zero" ΔE were determined as fitting parameters. The errors of the fitting parameters were found by decomposition of the statistical χ^2 function near its minimum, taking into account maximal pair correlations.

2.3. Electrochemical Measurements and Electrode Preparation. All electrochemical measurements were carried out using an Autolab PGSTAT 128N potentiostat/galvanostat in a three electrode electrochemical cell with three compartments in which the reference electrode compartment was connected to the working electrode compartment through a Luggin capillary and the counter electrode compartment separated from the working electrode compartment by a glass frit. An Ag/AgCl/KCl_{sat} electrode was used as a reference electrode where the potential in this work is referred to, whereas a platinum wire and a glassy carbon electrode were used as the counter electrode and substrate for the working electrode, respectively. Before use, the glassy carbon electrode was subjected to a cleaning procedure by polishing with an alumina slurry of 0.1 and 0.03 μm consecutively with the help of a polishing cloth and washing in an ultrasonic bath in ethanol/water and water each for 10 min, respectively.

The working electrode was prepared by dispersing 2.5 mg of the catalyst in 350 μL of a Nafion solution (5 wt % in lower aliphatic alcohols) and isopropanol (1/6, v/v) under sonication for 1 h followed by stirring for 2 h to obtain a homogeneous dispersion. A total of 5 μL of the catalyst dispersion was drop-coated on the glassy carbon substrate (A = 0.125 cm^2) and left

dx.doi.org/10.1021/cs401140g | ACS Catal. 2014, 4, 2449−2462

to dry in a saturated atmosphere of isopropanol at room temperature after which the working electrode was ready for electrochemical tests.

2.4. CO Stripping Measurements. CO stripping was used for determination of the electrochemical surface area. First, the catalyst was subjected to an electrochemical cleaning procedure by cycling the electrode in N_2 purged 0.5 M H_2SO_4 for 100 cycles in a potential window of −0.2 to 1 V at a scan rate of 100 mV s^{-1}. Then CO gas was purged into the solution for 20 min while holding the electrode potential at −0.15 V to allow for the adsorption of a monolayer of CO molecules. Afterward, dissolved CO was removed by purging the solution for 20 min with N_2 gas while keeping the electrode potential at −0.15 V. Finally, the voltammogram for CO stripping was recorded in a potential window of −0.15 to 0.9 V for three consecutive cycles. The first cycle is to record the CO_{ads} stripping and the next two cycles to ensure the complete stripping of CO_{ads} during the first cycle.

2.5. Methanol Oxidation Activity. Methanol oxidation was studied on all catalysts in 1 M CH_3OH/0.5 M H_2SO_4 using cyclic voltammetry and chronoamperometry. The prepared and previously electrochemically cleaned electrode was cycled in a potential window from −0.2 to 1 V at 100 mV s^{-1} for 200 cycles. The catalytic activity for all catalysts was compared at the 20th cycle, but the development of the catalysts activity during the potential cycling was also monitored. The methanol oxidation at a constant potential of 0.7 V was studied by chronoamperometry in 1 M CH_3OH/0.5 M H_2SO_4 for 1 h. A fresh electrode was prepared for this measurement and was subjected to the same electrochemical cleaning procedure as described above before recording the CA curve.

3. RESULTS AND DISCUSSION

3.1. Structural Characterization. *3.1.1. Metal Loading Determination by ICP.* The metal loadings of the prepared catalysts were determined by ICP analysis, and the results are shown in Table 2. Generally, the metal loading and the atomic ratios of the two components depend on the microwave irradiation mode and the irradiation duration. A clear dependence of metal loading on irradiation time is observed for the samples prepared under continuous irradiation. The amount of Pt increases from ca. 2% to ca. 10% when the time is increased from 40 to 90 s. Lower irradiation times of 40 and 50 s lead to comparably low amounts of Ni of ca. 1%, and this value increases to 2% with irradiation times of 60 s or higher. It should be noticed that the temperature of the reaction mixture during the microwave irradiation increased from 170 to 190 °C when the irradiation time increased from 50 to 60 s. The enhancement of Ni loading by increasing the irradiation time can be explained either by a larger rate of metal ion reduction at higher temperature or by the formation of higher amounts of Pt nanoparticles which may serve as seeds for Ni ion reduction.[35−37] With a further increase of the irradiation time from 60 to 90 s a slight decrease in Ni loading was observed, whereas Pt loading showed a slight increase. This behavior probably results from the galvanic displacement of Ni by Pt, i.e. the reduction of the more noble Pt ions forming metallic Pt by dissolving the less noble Ni (so-called redox exchange). Aging under stirring, which was intended to allow the PtNi particles to deposit on the support, has only a slightly beneficial effect on the metal loading. Equally aging under pH modification has been attempted to promote the deposition of the nanoparticles onto the carbon support.[38] Obviously, pH modification has an adverse effect on both the Pt and the Ni loading: they decreased after this step compared to the catalyst aged without pH modification (PtNi/CNT_C_90) or even the catalyst separated directly after the reduction process (PtNi/CNT_C_90_na). The decrease of metal loading as a result of pH modification in particular for Ni could be attributed to the dissolution of Ni under acid conditions.[39] The decrease of Pt loading after pH modification is more difficult to explain since dissolution of Pt is not expected under these conditions. The actual reason for the decreased Pt loading is not clear for us at the moment.

Table 2. Metal Loading and Atomic Ratios as Obtained from ICP and Particle Size from TEM

	metal loading [wt %]		atomic ratio		
PtNi/CNT catalysts	Pt	Ni	Pt	Ni	particle size [nm]
C_90_na	10.0	1.8	1.7	1	2.7
C_90_acid	7.6	0.7	3.1	1	3.2
C_90	10.2	2.0	1.5	1	3.3
C_60	9.8	2.3	1.3	1	2.8
C_50	7.4	1.0	2.2	1	n.d.
C_40	2.2	1.1	0.4	1	n.d.
P_6	7.5	0.8	3.0	1	2.5
P_9	8.1	1.6	1.5	1	4.7
P_12	10.0	1.9	1.6	1	2.5
P_18	10.2	2.2	1.4	1	2.7
Pt/C ETEK	19.5				3.1

As expected, for the catalysts prepared under pulsed microwave irradiation, the total metal loading increases with growing pulse number. The pulse mode provides obviously no advantage regarding the metal loading, since after 180 s of irradiation (i.e., 18 pulses) the loading is similar to that after 90 s of continuous irradiation. This behavior is the opposite of that reported by Song et al.,[40] where the efficiency was higher in the pulsed mode than in the continuous mode and which was discussed by the authors in view of the heating rate. In general, the heating rate can be correlated to the viscosity of ethylene glycol and its relaxation time.[41,42] Both viscosity and relaxation time influence the loss factor, which is a measure of conversion of microwave radiation into heat by the irradiated molecules.[43] Differences in the observed behaviors thus might be attributed to different temperature profiles and experimental conditions obtained in the different microwave setups.

In general, the total metal loading determined by ICP is lower than the theoretical one. The low Ni loading could be explained by the lower redox potential of Ni as compared to Pt, thus impeding the reduction of Ni by EG. It is, however, a challenge to prepare bimetallic catalysts containing non-noble elements with the microwave polyol method: A high pH should enhance the reduction of Ni ions[44] but at the same time could prevent the negatively charged nanoparticles from absorbing on the support.[45] Compared to the preparation of PtNi by the conventional polyol method,[32] the amount of Ni in the microwave assisted synthesis is higher, indicating that the higher temperature of microwave heating favors Ni ion reduction.[37]

3.1.2. XRD and TEM Characterization. The XRD patterns for the prepared catalysts are shown in Figure 1A−C. Figure 1A shows the XRD patterns for the catalysts prepared with continuous irradiation for 90 s under different aging conditions

dx.doi.org/10.1021/cs401140g | ACS Catal. 2014, 4, 2449−2462

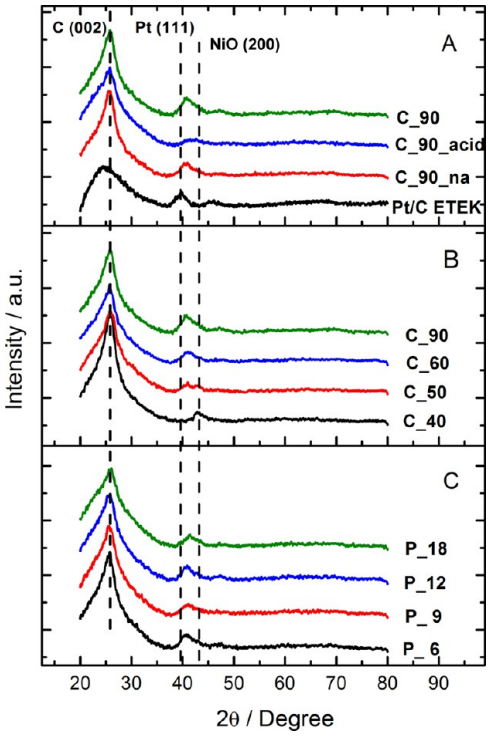

Figure 1. XRD patterns of PtNi/CNT electrocatalysts. (A) Effect of aging conditions, (B) effect of continuous irradiation duration, (C) effect of pulse number.

in comparison with the commercial Pt/C catalyst. The peak near $2\theta = 25°$ is assigned to graphite carbon in the support material. Importantly, the diffraction peaks of the prepared catalysts associated with the 111 plane are shifted to higher 2θ values (40.8°) in comparison to Pt/C (39.8°), indicating the formation of an alloy between Pt and Ni.[46−48]

The XRD patterns of catalysts prepared under continuous irradiation for different durations are shown in Figure 1B. PtNi/CNT_C_40 shows only a diffraction at $2\theta = 43°$ corresponding to the formation of NiO (200).[49,50] Since Pt in this catalyst was detected by ICP-OES, either the amount of Pt is too low to be detected with XRD or Pt particles initially formed are too small. Initial formation of Ni species is in agreement with our previous investigations on PtNi catalyst synthesis using conventional polyol reduction, where a preferential adsorption of Ni ions on the oxidized CNT surface has been postulated.[32] A high initial deposition rate of Ni simultaneously with a low Pt deposition rate would be counterintuitive given the lower redox potential of Ni as compared to Pt. The exact deposition mechanism is not clear to us at the moment, and we could only speculate on kinetic effects facilitating the reduction of surface-bound Ni ions. Small Ni particles formed initially might be oxidized during handling in air after synthesis and are thus found as NiO in XRD. It cannot finally be ruled out that $Ni(OH)_2$ precipitates during impregnation and is converted into NiO during drying. However, it would then be hard to explain why these species should disappear after prolonged irradiation (see below). Upon increasing the irradiation time to 50 s, a new diffraction peak adjacent to the NiO peak develops at 2θ (40.8°) assigned to PtNi alloy formation. Further increasing the irradiation time to 60 and 90 s increases the intensity of the PtNi diffraction peak, whereas the NiO peak vanishes completely, probably indicating that the initially formed Ni nuclei may serve as basis for the formation of the alloy.

For the catalysts prepared with pulsed irradiation (PtNi/CNT_P, Figure 1C), the pulse number has only slight effects on the crystal structure. NiO cannot be detected even at low pulse numbers; however, it cannot be excluded that initially NiO is present, which is converted into PtNi alloy already after six pulses (i.e., 60 s), as suggested by the results from continuous irradiation. All catalysts show a shift to higher 2θ values than that of Pt, and the shift is more pronounced in the sample prepared at 18 pulses (PtNi/CNT_P_18), indicating a higher alloying extent.

Conventional TEM images of selected catalysts are shown in Figures 2 and 3; additional images can be found in the Supporting Information (Figures S2 and S3). Particle sizes determined from TEM are summarized in Table 2. The catalysts prepared with continuous irradiation (Figures 2A and B) contain small particles well dispersed on the CNT support. Increasing the irradiation time or aging the catalyst under stirring overnight (PtNi/CNT_C_90) increases the particle size from 2.7 to 3.3 nm with simultaneous appearance of regions with some agglomeration. On the other hand, acidification of the reaction medium after the reduction process (PtNi/CNT_C_90_acid) followed by aging results in high dispersion of the nanoparticles on the CNTs while keeping the same particle size (3.2 nm). It is expected that at lower pH the surface of CNTs is positively charged by protonation of basic surface functional groups, and therefore the nanoparticles protected by adsorbed negatively charged glyconate ions formed during reduction can be adsorbed on the surface of the CNTs with high dispersion.

The catalysts prepared under pulsed irradiation (PtNi/CNT_P, Figure 3A and B) exhibit particle sizes virtually independent of the number of pulses (about 2.5 nm), as demonstrated for the samples PtNi/CNT_P_6 (Figure 3A) and PtNi/CNT_P_18 (Figure 3B). The sample PtNi/CNT_P_9 is an exception with a particle size of 4.7 nm (Figure S3A). Increasing the pulse number and therefore the irradiation time enhances the presence of agglomerated particles as indicated by a comparison of Figure 3A and B.

3.1.3. XPS and XAFS Characterization. The Pt (4f) photoelectron spectra of selected PtNi catalysts compared with Pt/C are presented in Figure 4A. The Pt (4f 7/2) signal of the monometallic sample has a BE of 71.9 eV, which is somewhat higher than that of bulk Pt (71 eV).[51,52] The pronounced line asymmetry is typical of the metallic state; therefore this shift to higher energies is most likely not related to a higher Pt oxidation state but to initial-state or final-state effects due to small particle size[53,54] or influences of the support. The ca. 0.4 eV shift to lower binding energies in the Pt−Ni catalysts is similar to what has been observed in an earlier study on Pt−Ni catalysts.[32] Such shifts are often interpreted as arising from alloy formation, but we hesitate to do so due to the multiplicity of possible influences on XPS binding energy in this complex system.

The Ni 2p XPS spectra are presented in Figure 4B. Although the Ni signals are weak, some conclusions on the nickel state can be derived. In all samples, the Ni^{2+} state with a BE of ca. 856.2 eV can be detected together with its characteristic broad shakeup satellite approximately 4 eV higher. A contribution from the Ni metallic state can also be detected in all samples. The deconvolution of the Ni 2p signal is illustrated for PtNi/CNT_C_90 in Figure 4C, while the Ni to Pt and Ni^0/Ni^{2+}

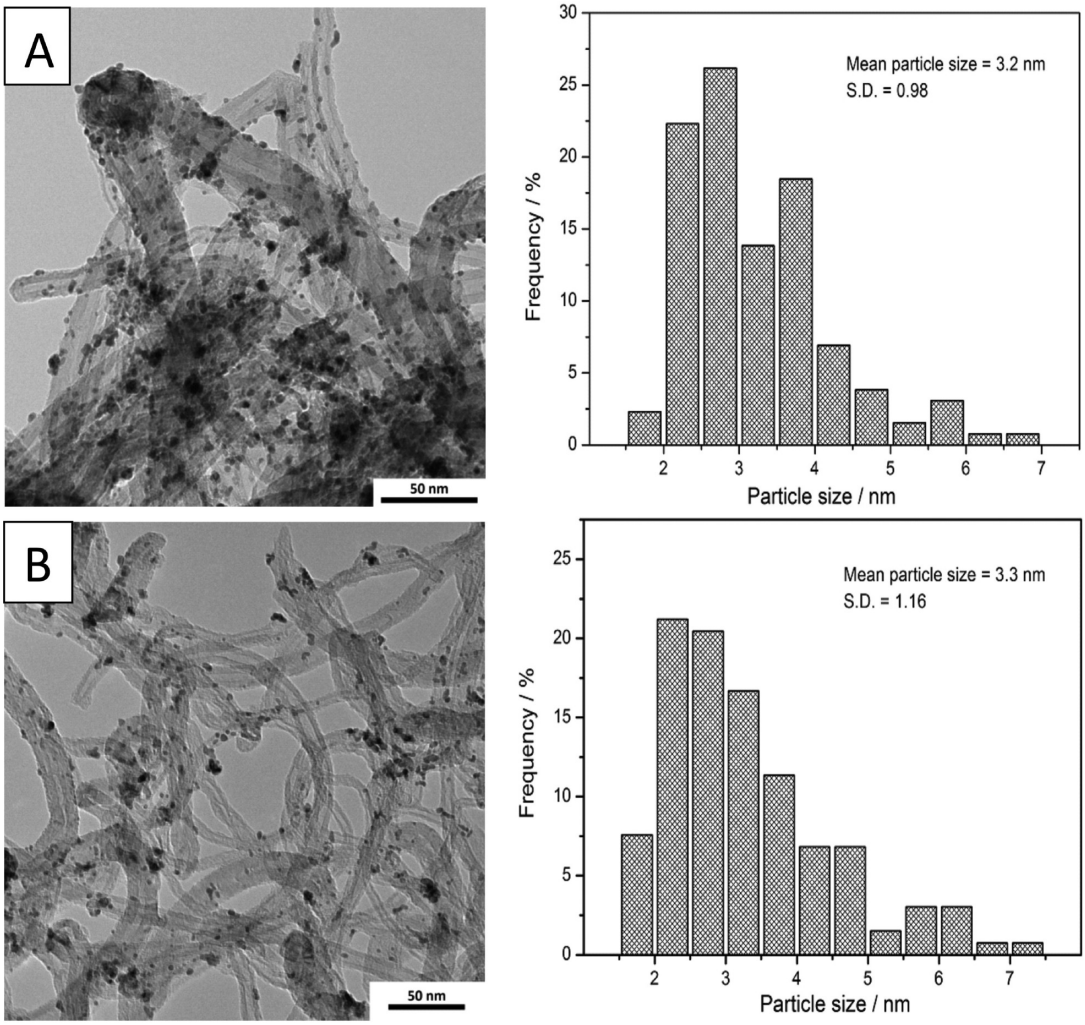

Figure 2. TEM images of PtNi/CNT_C electrocatalysts. (A) PtNi/CNT_C_90_acid, (B) PtNi/CNT_C_90.

ratios from XPS signal deconvolution are summarized in Table 3. It can be seen that most of the samples are severely oxidized, while aging under the addition of acid leads to a significant increase of metallic Ni contribution accompanied by an overall decrease in nickel content. This behavior agrees well with the ICP results discussed above where the total Ni content decreases upon acid treatment due to Ni dissolution. The higher contribution of metallic Ni in PtNi/CNT_C_90_acid as detected from XPS indicates that Ni oxide species including NiO are dissolved preferentially in the acidic medium. It is quite possible that the Ni ions accessible to the acid were completely dissolved during aging, but further oxidation of surface species happened during sample storage. The surface Ni content detected with XPS is slightly lower than the bulk one measured by ICP-OES for all samples with the exception of PtNi/CNT_P_12, which may indicate a tendency of Pt to occupy the surface of the catalyst particle where Ni tends to be more concentrated near the oxidized support during the preparation process as reported in ref 32.

The Pt L_3-edge X-ray absorption near edge structures (XANES) are shown in Figure 5A. The absorption at 11.564 keV corresponds to the $2p_{3/2}$−5d electronic transition of Pt metal, and the amplitude of the first feature at ca. 11.569 keV, known as the white line (WL), reflects the orbital occupancy of the 5d electronic state. The WL intensity increases with decreasing occupancy in the 5d orbital. Figure 5A shows that the white line intensities for all samples are slightly higher than that of a Pt foil. As it was reported before,[55] both oxidation state and alloying of platinum can cause changes in WL intensity. Since no significant oxidation of the platinum outer layers was detected by XPS and the presence of oxidized Pt in the bulk of the particles is highly unlikely, one can conclude that the WL intensity changes observed are an effect of Pt−Ni alloy formation. The Pt L_3-edge Fourier Transformed (FT) EXAFS spectra are depicted in Figure 5B. In the spectra, signals can be discerned between 1.7 and 3.25 Å (uncorrected), the interpretation of which requires modeling of the coordination sphere. The fact that the scattering intensity ranges down to 1.7 Å (uncorrected) shows the presence of light neighbors—oxygen or carbon—in the coordination sphere of Pt. The spectra were fitted using three different shells for next neighbors (Pt, Ni, and O representing the light backscatterer), and the results are collected in Table S1 (see the Supporting Information). In Figure 5C, a typical fit is shown to demonstrate the fit quality, while the most important data (CN, r) are summarized in Table 4 together with platinum pairing factors P_{Pt}. The latter are calculated according to $P_{Pt} = CN_{Pt-Ni}/(CN_{Pt-Ni} + CN_{Pt-Pt})$, where CN_{i-j} are coordination numbers of element j in the first coordination sphere of

dx.doi.org/10.1021/cs401140g | ACS Catal. 2014, 4, 2449−2462

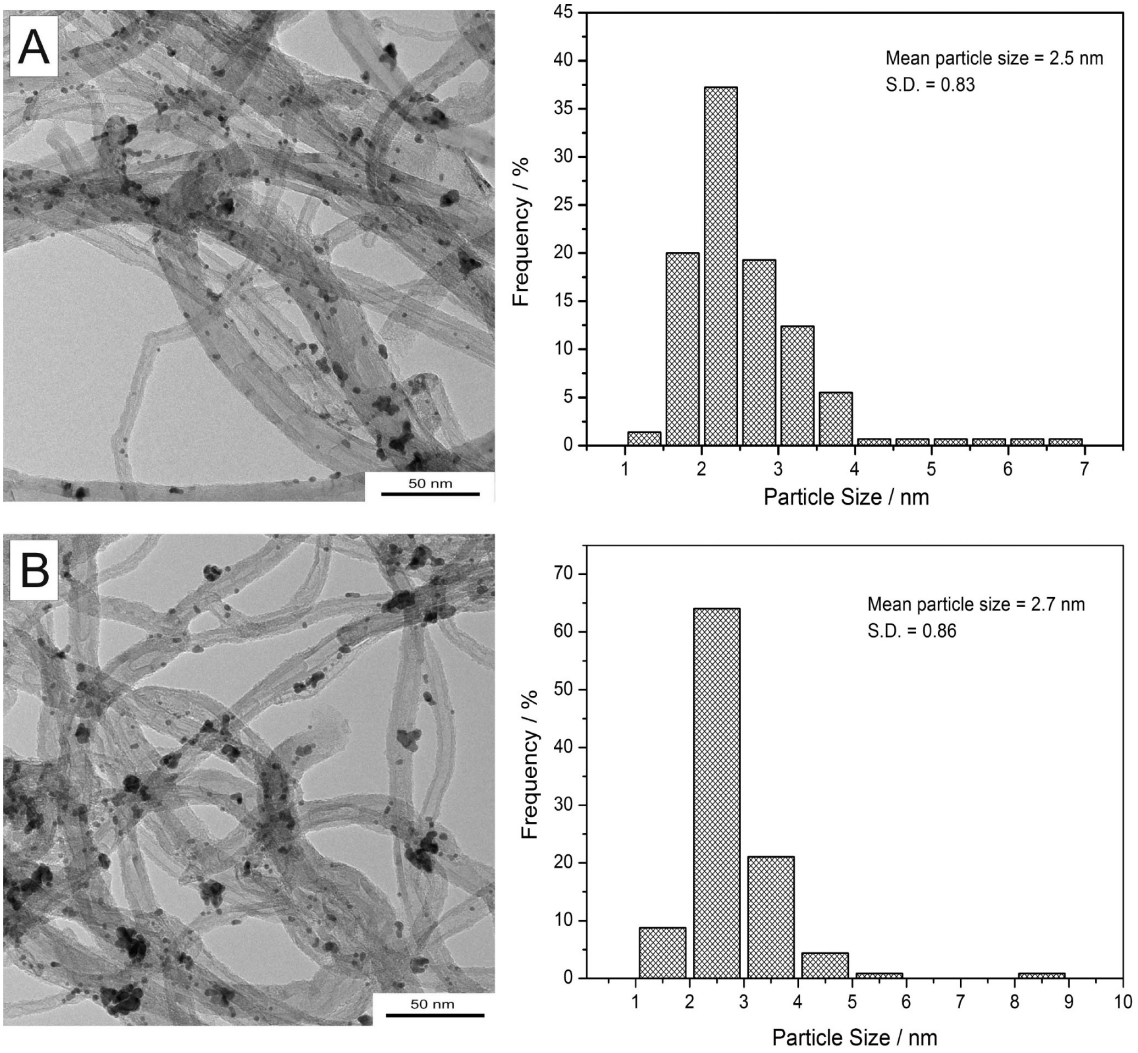

Figure 3. TEM images of PtNi/CNT_P electrocatalysts. (A) PtNi/CNT_P_6 and (B) PtNi/CNT_P_18.

element *i*. They allow judging on the degree of segregation and mixing in an alloy particle.[56]

In the fits, Pt−Ni CN was found to range between 1 and 1.6, which is a clear proof of alloy formation. The distance between Pt and the light scatterer "O" is consistently between 2.03 and 2.05 Å, which is significantly below the sum of covalent radii of Pt (1.39 Å) and O^{2-} (0.72 Å). This neighbor is therefore support carbon rather than oxygen. The fact that support carbon can be seen in the EXAFS spectra suggests a very small particle size or raft-like particle morphologies. The sum of CN of Pt with both metals, Pt and Ni, is consistently between 6.2 and 6.5 except for sample PtNi/CNT_C_90_acid, which was aged in acid. This also suggests extremely small average sizes of the primary particles, probably below 1 nm. This is in good agreement with HR-TEM images, which show that the larger catalyst particles are aggregates of such small primary particles (see below). PtNi/CNT_C_90_acid displays an even lower total coordination number, indicating an even smaller average particle size. The disagreement of this result with the TEM images may arise from the most likely polycrystalline nature of the particles seen in the microscope. Platinum pairing factors are generally very small (0.19−0.26), which indicates poor mixing between Pt and Ni. This is consistent with results obtained in a recent study with catalysts prepared by the conventional polyol route,[32] where coordination numbers and pairing factors were extracted from both Ni K and Pt L_3 EXAFS, the latter being ∼0.2. In this case, it was shown by combination of both surface sensitive (XPS, ISS) and bulk techniques (XRD, TEM, and XAS) that the Pt−Ni nano alloys had a homophilic structure with Ni concentration rising toward the metal−support interface. The similar pairing factors of platinum in the present case as well as the relatively small Ni/Pt ratios obtained by XPS as compared to ICP suggest that the particle model proposed in ref 32 might be valid also for the present catalysts made by microwave-assisted preparations. It should be noted that our PtL_{III} edge EXAFS spectra cover only Ni species that have Pt neighbors, i.e., Ni species in or at the surface of alloy particles. The latter may be oxidized. NiO phases as detected by XRD are not seen in these measurements. As the coexistence of segregated and alloy phases would strongly complicate the interpretation of Ni *K* XAFS results, such data were not measured for the present series. While the segregated Ni phases are most likely dissolved in the pretreatments prior to electrochemical measurements, the Pt-related Ni atoms are more likely to survive, except perhaps for surface atoms.

3.1.4. HR-TEM/STEM-EDX. To gain additional insight into the structural features of the catalysts, HR-TEM as well as

dx.doi.org/10.1021/cs401140g | *ACS Catal.* 2014, 4, 2449−2462

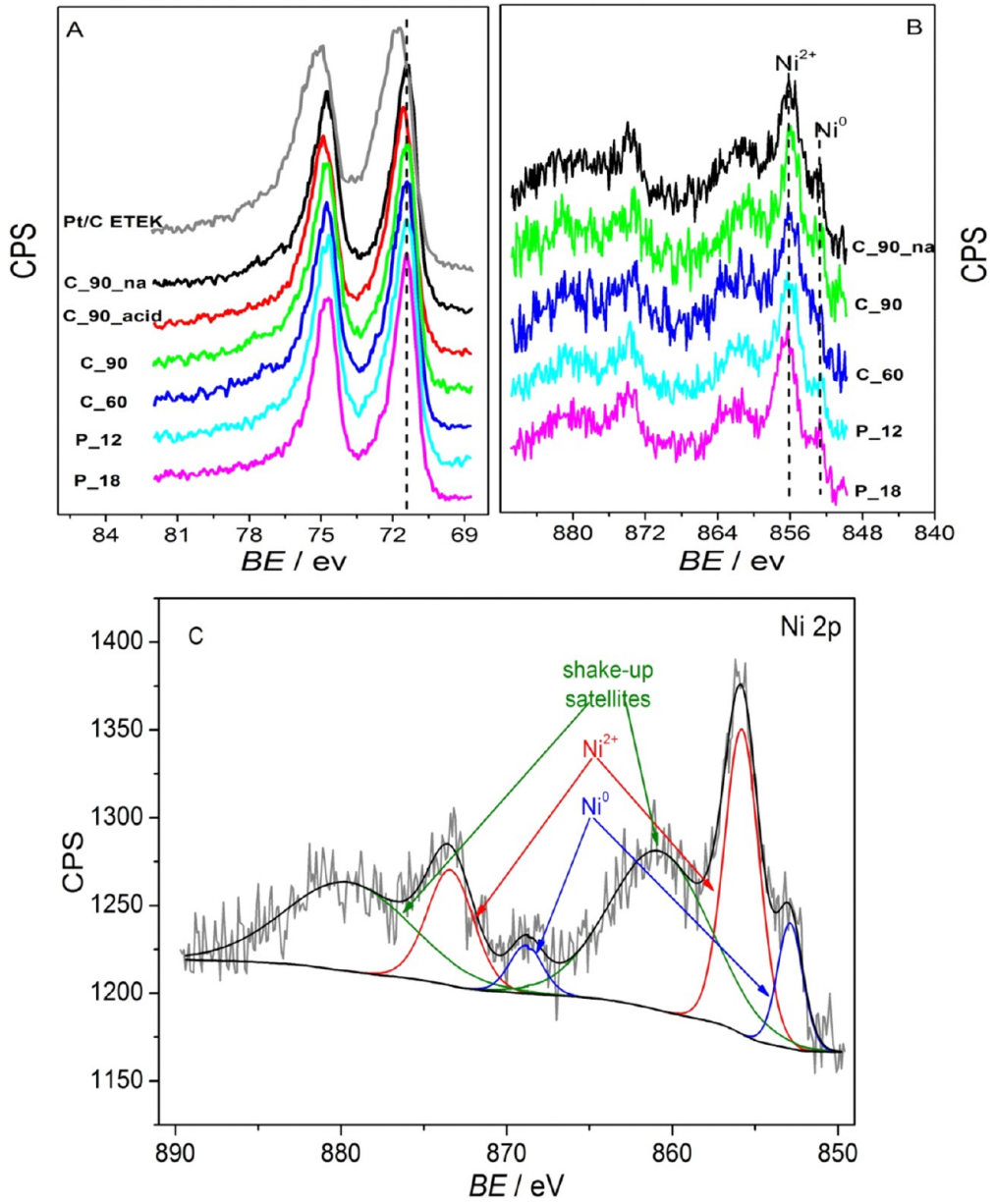

Figure 4. XPS spectra of PtNi/CNT electrocatalysts. (A) Pt 4f signals, (B) Ni 2p signals (Ni 2p spectrum of PtNi/CNT_C_90_acid is not shown due to lower signal-to-noise ratio), and (C) Ni 2p deconvolution exemplified with the PtNi/CNT_C_90 sample.

Table 3. Atomic Ratios as Calculated from XPS

PtNi/CNT catalysts	C_90_na	C_90_acid	C_90	C_60	P_12	P_18
Ni^0/Ni^{2+}	0.09	0.29	0.11	0.05	0.08	0.16
Ni/Pt XPS	0.53	0.20	0.60	0.63	0.66	0.68
Ni/Pt ICP	0.58	0.32	0.66	0.77	0.63	0.71

STEM combined with EDX has been carried out on selected samples. Representative images are shown in Figures 6 and 7. In both samples, particles can be found which seem to consist of accumulated very small primary particles. The impression is that these primary particles are not just agglomerated but are grown together to a large extent. However, larger agglomerates, as seen already in conventional TEM, are also present. These observations would be in line with heterogeneous particle growth where small primary particles initially form, onto which additional particles deposit. Both Figures 6 and 7 clearly indicate that the element distribution in the particles is inhomogeneous. There is an accumulation of Ni toward the center of particles or toward one side of the particle.

3.2. Electrochemical Characterization. *3.2.1. CO Stripping and Surface Area Determination.* CO stripping was used to determine the electrochemical surface area of the catalysts of this study. Representative CO stripping voltammograms are shown in Figure 8. Peak potentials for CO oxidation are summarized in Table 5. CO adsorption is confirmed by the absence of hydrogen desorption peaks in the lower potential region of the first cycle. During the positive potential sweep, a shoulder at around 0.5 V followed by a signal at 0.59 V resulting from CO oxidation is visible. During the second cycle, the voltammograms don't show any peak for CO oxidation, while the formation and oxidation of H_{upd} is clearly visible, indicating that CO_{ads} was oxidized completely during the first scan. We want to emphasize that there was no significant potential shift for the CO oxidation peak on the PtNi catalysts

dx.doi.org/10.1021/cs401140g | ACS Catal. 2014, 4, 2449−2462

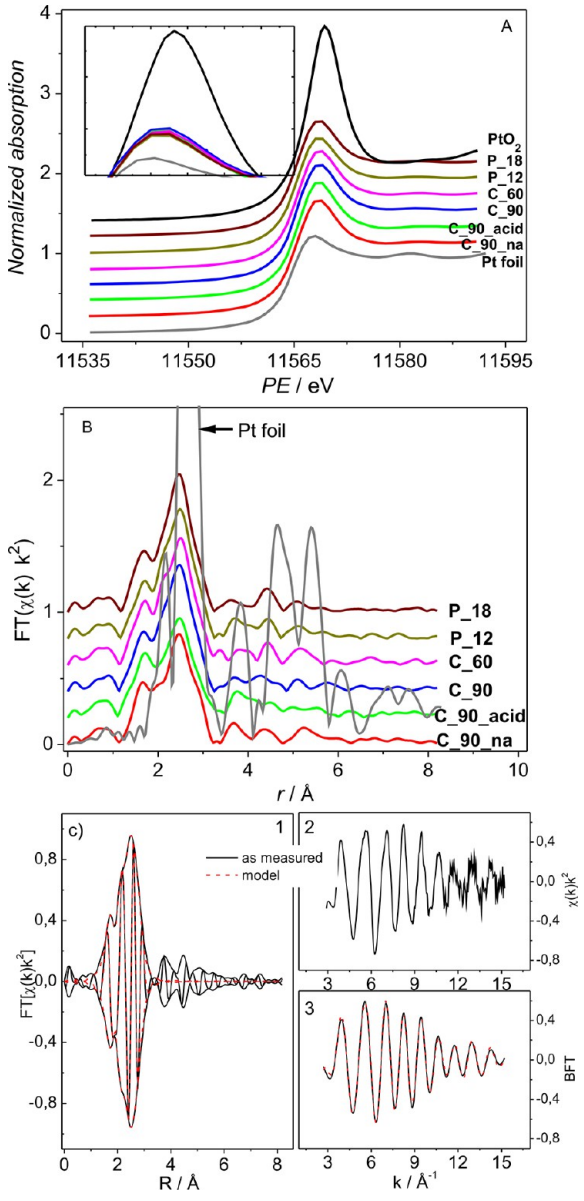

Figure 5. Pt L_3-edge XANES spectra (A) of the PtNi/FCNTs together with Pt-foil and PtO_2 references, Pt L_3-edge FT-EXAFS spectra (B) of the PtNi/FCNTs together with Pt-foil reference and their fit three shell model exemplified by PtNi/CNT_P_12 (C).

Table 4. PtL_3 EXAFS Fitting Parameters—Coordination Numbers and Distances (in Brackets, in Å) along with Total Coordination Numbers CN_{total} and Platinum Pairing Factors P_{Pt}

PtNi/CNTs catalysts	C_90_na	C_90_acid	C_90	C_60	P_12	P_18
Pt–O	1.37 (2.05)	1.55 (2.05)	1.13 (2.03)	1.19 (2.04)	0.97 (2.04)	1.11 (2.04)
Pt–Ni	1.25 (2.69)	0.98 (2.69)	1.56 (2.67)	1.62 (2.66)	1.67 (2.67)	1.60 (2.68)
Pt–Pt	5.29 (2.74)	4.2 (2.74)	4.72 (2.73)	4.57 (2.74)	4.85 (2.74)	4.92 (2.73)
CN_{total}	6.5	5.2	6.3	6.2	6.5	6.5
P_{Pt}	0.19	0.19	0.25	0.26	0.26	0.25

in comparison to Pt/C (compare Table 5). This behavior could be attributed to the fact that the surface of PtNi catalysts

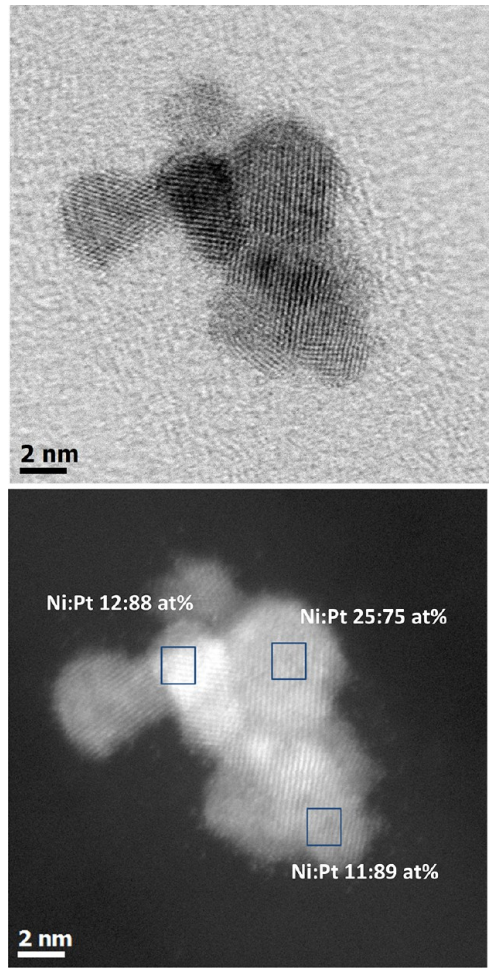

Figure 6. HR-TEM (upper) and STEM-EDX images of PtNi/CNT_C_90. The local atomic Ni:Pt composition as determined from EDX is indicated for the selected area.

resembles a Pt surface as a result of catalyst restructuring/Ni dissolution during the pretreatment of PtNi catalysts (electrochemical treatment in an acid environment for 100 cycles, compare Figure S4A).[57]

The electrochemical surface area of the catalysts under investigation has been evaluated from the integration of the charge consumed during the CO stripping after correction for the double layer and anion adsorption related currents:

$$\mathrm{ECSA}\ (\mathrm{cm}^2_{\mathrm{Pt}}) = \frac{Q_{\mathrm{CO}}}{Q_0} \tag{7}$$

where Q_{CO} is the integrated charge consumed during the CO_{ads} oxidation and Q_0 is the standard charge required for oxidation of a CO_{ads} monolayer on a Pt surface with a value of 420 μC cm^{-2}.

The specific electrochemical surface area (SECSA; $m^2\ g_{pt}^{-1}$) was calculated by dividing the electrochemical surface area obtained from eq 7 by the platinum loading on the electrode (L_{Pt}, calculated based on the experimentally (ICP-OES) determined Pt loading) according to the following equation:

$$\mathrm{SECSA}\ (\mathrm{m}^2/\mathrm{g}_{\mathrm{Pt}}) = \frac{\mathrm{ECSA}}{L_{\mathrm{Pt}}} \tag{8}$$

The calculated specific surface area of the catalysts under investigation is shown in Table 5. For catalysts prepared under

dx.doi.org/10.1021/cs401140g | ACS Catal. 2014, 4, 2449–2462

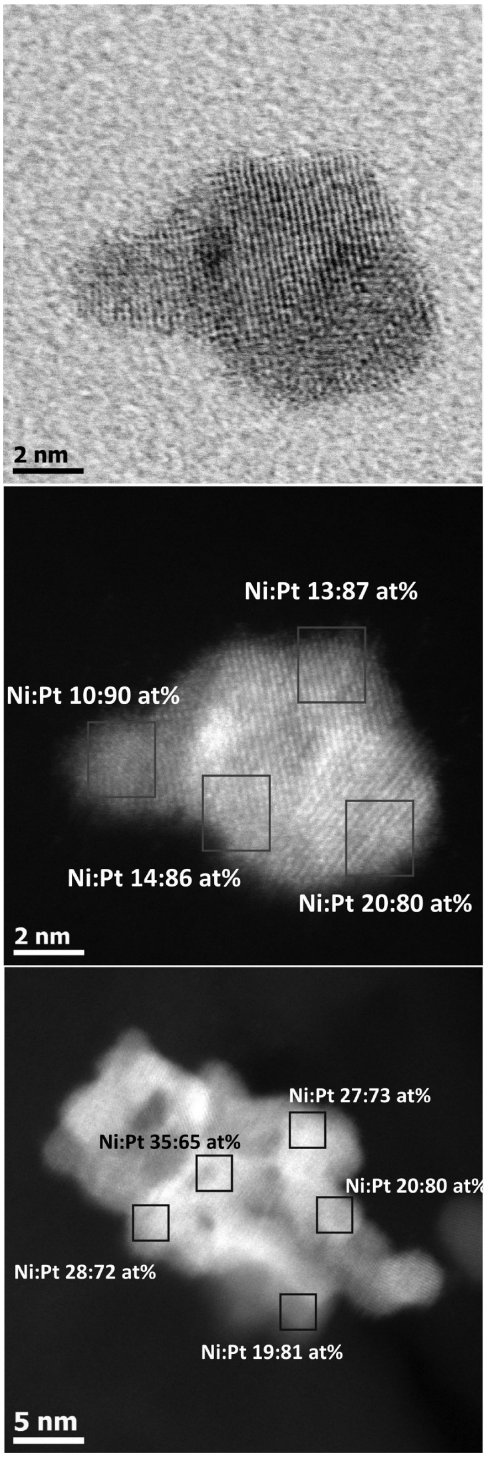

Figure 7. HR-TEM (upper) and STEM-EDX images of PtNi/CNT_P_18. The local atomic Ni:Pt composition as determined from EDX is indicated for the selected area.

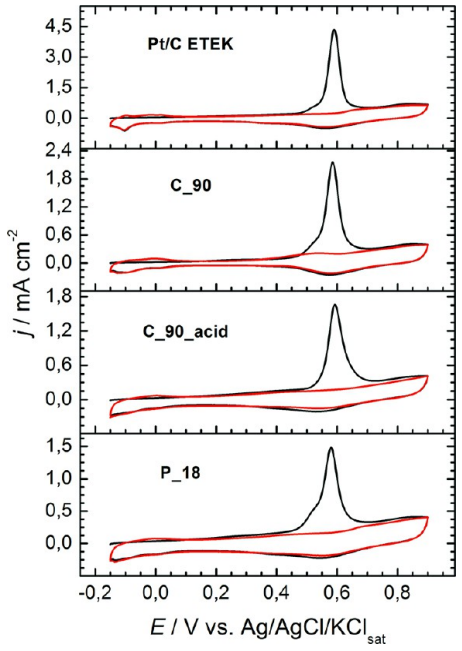

Figure 8. CO stripping voltammograms of selected PtNi/CNT catalysts in 0.5 M H_2SO_4, scan rate 20 mV s^{-1}.

continuous irradiation, the specific surface area increases with irradiation time. The catalyst aged in acidified media (PtNi/CNT_C_90_acid) shows slightly higher SECSA probably resulting from the dissolution of Ni and/or NiO surface species under formation of a Pt/PtNi skeleton structure. The catalyst prepared at 40 s of irradiation time (PtNi/CNT_C_40) behaves different in CO stripping and CV showing high electrochemical surface area which might probably be attributed to the presence of only small Pt particles (see above, XRD).

For the catalysts prepared in pulsed irradiation mode, the change of the SECSA was small except for the catalysts PtNi/CNT_P_9, which showed higher SECSA that could be attributed to the high dispersion and the absence of nanoparticle agglomeration in this catalyst, although it has the highest particle size among all PtNi/CNT_P catalysts (Figure S3A). The reason for this different behavior is not clear to us at present.

In general, with proper control of the conditions during microwave preparation, we were able to prepare PtNi/CNT catalysts in very short time with high specific electrochemical surface area comparable to that of Pt/C ETEK and to that of other PtNi/C catalysts reported in the literature[17,46,58] and higher than that of PtNi/FCNTs prepared by the conventional polyol method (SECSA of 29.1 m^2 g_{Pt}^{-1}).[32]

3.2.2. Methanol Oxidation Activity. To evaluate the catalytic activity of the prepared catalysts toward methanol electrooxidation, they were tested in 1 M CH_3OH/0.5 M H_2SO_4 solution using cyclic voltammetry. Typical voltammograms are shown in Figure 9. In these figures, the current is given per mass of Pt. CVs showing the surface-specific currents can be found in the Supporting Information (Figure S5). The CVs for methanol oxidation on PtNi catalysts resemble that of Pt/C catalysts[32,46,47,59] with a forward and a backward anodic peak. The ratio of peak current in the forward and in the backward scan (I_f/I_b) is typically considered as a measure for the poisoning resistance of a catalyst: on a less-poisoned catalyst,[60] the current in the forward scan may be higher than on a strongly poisoned one, thus leading to a higher I_f/I_b ratio. Since our catalyst model (see below) includes a Pt-enriched shell and dissolution of outer Ni species, we assume that this higher poisoning tolerance is not due to enhanced water activation but due to weaker CO bonding, in line with the decreased d-band occupancy as detected from XANES. However, it can also not completely be excluded that these

dx.doi.org/10.1021/cs401140g | ACS Catal. 2014, 4, 2449−2462

Table 5. Electrochemical Parameters from CO Stripping and CV Measurements

PtNi/CNTs catalysts	peak potential CO oxidation [mV]	SECSA [$m^2\ g_{Pt}^{-1}$]	peak potential MeOH oxidation [mV]	MSA [$mA\ mg_{Pt}^{-1}$]	SSA [$mA\ cm_{Pt}^{-2}$]	I_f/I_b
C_90_na	0.584	43.4	0.676	524.2	1.20	0.8
C_90_acid	0.593	51.1	0.673	474.6	0.93	1.0
C_90	0.585	48.1	0.688	618.5	1.28	0.78
C_60	0.580	37.1	0.679	628.8	1.69	0.75
C_50	0.590	30.3	0.669	486.7	1.60	0.78
C_40	0.590	87.9	0.660	682.2	0.77	1.1
P_6	0.586	33.7	0.670	468.9	1.39	0.81
P_9	0.582	47.1	0.675	570.2	1.20	0.86
P_12	0.589	31.3	0.673	471.0	1.50	0.82
P_18	0.580	36.1	0.679	582.9	1.62	0.81
Pt/C ETEK	0.590	45.7	0.690	482.5	1.05	0.60

changes in d-band structure influence water activation. The I_f/I_b values are shown in Table 5, and it can be seen that all PtNi samples show higher poisoning resistance than the reference Pt/C E-TEK catalysts. The catalytic activities as shown in Table 5 were determined as mass specific activity (MSA) and surface specific activity (SSA), as given by eqs 9 and 10:

$$\mathrm{MSA} = \frac{I_{\mathrm{peak}}}{L_{\mathrm{Pt}}} \tag{9}$$

$$\mathrm{SSA} = \frac{I_{\mathrm{peak}}}{\mathrm{ECSA}} \tag{10}$$

Table 5 indicates that the SSA for all PtNi/CNT catalysts is higher than that of the Pt/C sample with the exception of PtNi/CNT_C_90_acid and PtNi/CNT_C_40. The reason for the comparably lower activity of PtNi/CNT_C_90_acid might be the low Ni surface content (compare Table 3). In our previous paper,[32] we speculated on the necessity of having active sites with a certain atomic arrangement of Pt and Ni atoms, i.e., at least three adjacent Pt sites for methanol adsorption/dehydrogenation[14] in close contact with a Ni atom, and the number of such sites might be low in PtNi/CNT_C_90_acid with low Ni content. On the other hand, the I_f/I_b ratio of PtNi/CNT_C_90_acid is exceptionally higher, indicating lower poisoning susceptibility. This could be attributed to the formation of low coordinated Pt atoms as result of acid dissolution followed by the electrochemical pretreatment. Such low-coordinated Pt atoms are considered as active sites for water activation and therefore CO removal.[61] More facile removal of CO will result in a lower degree of poisoning. Similarly, the catalyst PtNi/CNT_C_40 has a rather high I_f/I_b value, probably attributable to small Pt particle size. Generally, the surface specific activities of the PtNi/CNT_C and PtNi/CNT_P catalysts are within 1.2 and 1.69 mA/cm^2. There is a slight trend to higher SSA with higher pulse number which might be attributed to a higher Ni content in these catalysts (compare Table 2). For the MSA generally, it can be observed that the PtNi/CNT_P catalysts display higher activity than that of Pt/C but lower than the highly active PtNi/CNT_C catalysts (PtNi/CNT_C_90 and PtNi/CNT_C_60), which is somehow surprising given the slightly lower particle sizes in the PtNi/CNT_P catalysts. There are several factors that influence methanol oxidation on these catalysts including particle size and shape and Ni surface and bulk atomic ratio. The intricate interplay between these factors might lead to the observed variation in MSA.

From a practical point of view, where the MSA is relevant, the continuous mode of irradiation is more effective in preparing nanoparticle catalysts using the microwave-assisted polyol method than the pulsed mode. In general, the optimized catalysts reported in this study showed higher MSA, up to 1.5 fold than that obtained with PtNi/FCNTs (1:1) catalysts prepared by us via the conventional polyol method[32] and also higher than the activity of PtNi catalysts reported recently by other groups.[17,46,59]

To evaluate the stability of the catalysts during potential cycling in CV measurements, the variation of MSA with cycle number is shown in Figure S6 for two selected catalysts: PtNi/CNT_C_90 and PtNi/CNT_P_18. Additionally, the values normalized to the initial current are displayed. Both catalysts display similar behavior as they show an initial decrease in the activity which declines with increasing cycle number. From the normalized currents, it can be seen that both catalysts retain almost 82% of the initial current value after 200 cycles.

The catalyst stability was also tested in CH_3OH/H_2SO_4 and compared to Pt/C using chronoamperometry at 0.7 V for 1 h. The chronoamperometric curves are shown in Figure 10. The catalysts prepared at different irradiation times (Figure 10A) show almost the same stability, which is higher than that of Pt/C ETEK, whereas the catalysts PtNi/CNT_C_40 shows the lowest stability. As discussed above, this catalyst contains high amounts of NiO which probably dissolves with time, leading to lower activity. Among the PtNi/CNT_P catalysts (Figure 10B), the catalyst prepared at the highest pulse number (PtNi/CNT_P_18) shows the highest stability, whereas the other catalysts are close to Pt/C.

Compared to the recently reported steady state currents after 1 h at the same potential (0.896 V vs NHE) for PtNi (1:1) supported on PDDA modified carbon black, graphene, and PDDA modified graphene, with currents of 4.4, 32.7, and 64.3 $mA\ mg_{Pt}^{-1}$, respectively,[62] our catalysts (PtNi/CNT_C_90, PtNi/CNT_C_60, PtNi/CNT_C_50, PtNi/CNT_P_18) show higher stability with steady state currents of 79.8, 88.5, 79.8, and 84.18 $mA\ mg_{Pt}^{-1}$, respectively. Pt/C E-TEK exhibits a steady state current of 55.4 $mA\ mg_{Pt}^{-1}$.

Additionally, the chronoamperometric curves with current expressed in terms of surface specific current are shown in Figure S7A and B. The same behavior as in Figure 10A and B is observed.

3.3. Origin of the Activity Enhancement in PtNi/CNT Catalysts and Model of the Catalyst Structure. In a bimetallic catalyst system, the catalytic activity always depends on the surface arrangement of the two active components of

dx.doi.org/10.1021/cs401140g | ACS Catal. 2014, 4, 2449−2462

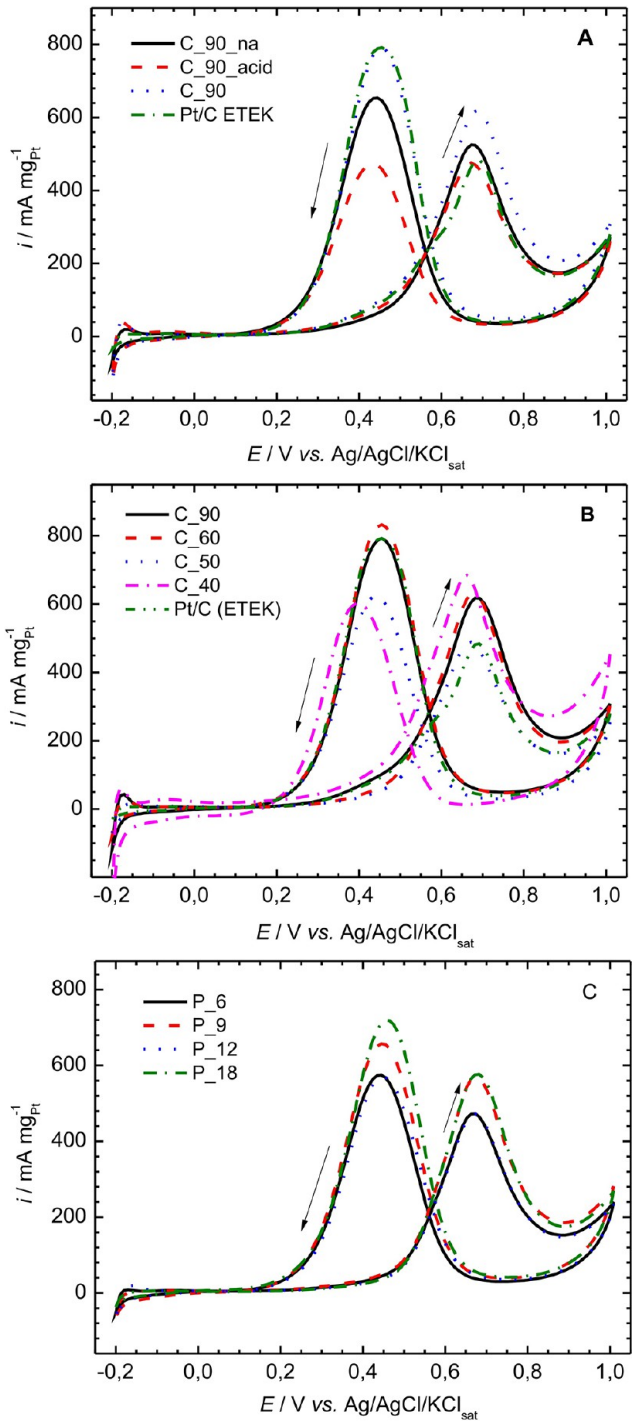

Figure 9. CVs of PtNi/CNT electrocatalysts in 1 M CH_3OH/0.5 M H_2SO_4 scan rate 100 mV s^{-1}; current normalized to the Pt loading in the electrode. Arrows indicate scan direction.

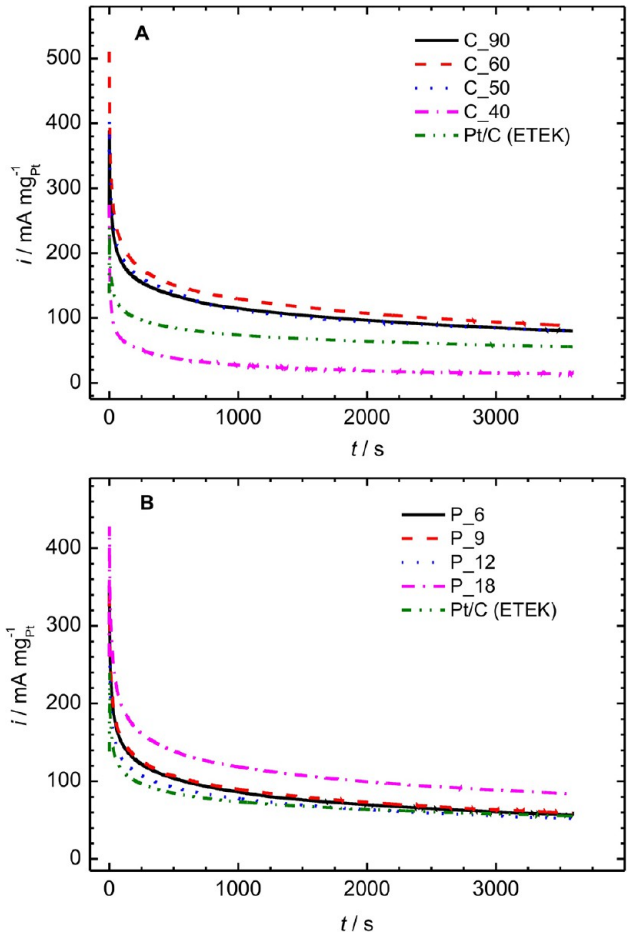

Figure 10. CA curves of PtNi/CNT electrocatalysts in comparison with Pt/C ETEK in 1 M CH_3OH/0.5 M H_2SO_4 at 0.7 V; (A) effect of irradiation time and (B) effect of pulse number.

the system. Two mechanisms are suggested to explain the enhancement of methanol oxidation and CO tolerance in bimetallic Pt−M catalysts. The first mechanism is the bifunctional mechanism which requires that the second metal be adjacent to Pt on the surface, where the Pt catalyzes the methanol adsorption and dehydrogenation resulting in the formation of adsorbed CO intermediates, and the second metal supplies the oxygen species to oxidize the adsorbed CO. The second mechanism is the electronic effect in which the second metal modifies the electronic properties of Pt, reducing CO bonding energy and enhancing CO tolerance.

For our catalyst system, the following structural model can be derived. Based on our XPS and ICP-OES analysis, the catalysts after synthesis show Pt-enriched surfaces with lower amounts of Ni on the surface. On the other hand, XRD, XPS, and XAFS analyses confirmed alloy formation in PtNi as detected from a Pt diffraction peak shifting in XRD, a Pt 4f signal shifting in XPS, and changes in the white line intensity in XANES. However, still some Ni/NiO species are detectable on the catalyst surface. Thus, the as-prepared catalyst comprises a PtNi core surrounded by a Pt-enriched shell with additional Ni species. HR-TEM/STEM-EDX images are in line with these observations but also demonstrate that the catalysts do not consist of single crystalline particles but of multicrystalline ones, which are probably grown in a heterogeneous nucleation process with enrichment of Ni to one side or the center of the particle. The electrochemical treatment of the catalysts in acid solution before testing the catalytic activity is expected to dissolve all Ni surface and subsurface species further evolving a structure with a strongly Pt-enriched surface where a PtNi alloy is in the core as confirmed from the base voltammograms of the catalysts (Figure S4).[57] It is likely that the electrochemical treatment in acid solution results in increasing Pt surface and formation of a thick layer with lower coordinated sites.[58] Similar behavior is expected for the catalysts when treated first with acid followed by electrochemical treatment as the acid can

dx.doi.org/10.1021/cs401140g | ACS Catal. 2014, 4, 2449−2462

dissolve the Ni and NiO forming a Pt-enriched surface with skeleton structure of Pt/PtNi. The acid treatment was carried out in nitric acid overnight under stirring, which should affect the catalysts structure as a result of acidic dissolution of Ni. Further electrochemical treatment should lead to additional Ni dissolution. Both dissolution mechanisms should be different, since the first one is a purely chemical one and the second one associated with additional electrochemical stress. Thus, for the electrochemical dissolution step, the as prepared sample and the leached sample provide different starting materials. However, it is expected that Ni from the PtNi alloy core will, for both the acid treated and the nonacid treated samples, undergo further slow dissolution, finally resulting in a thermodynamically stable PtNi core surrounded by a Pt enriched shell. Thus, it cannot be excluded that after long-term electrochemical treatment both chemically leached and nonleached samples will result in the same material.

From this model of the catalyst structure, we can expect that the bifunctional mechanism is not suitable to discuss the enhancement of electrocatalytic activity in our PtNi catalysts, since no Ni sites seem to be in direct contact with the electrolyte for water activation. Thus, an electronic effect is suggested. The increase in white line intensity and the direction of the XPS line shift seem to be contradictory, the former indicating electron deficiency, the latter electron abundance, but it should be noted that both phenomena are complex effects that are also influenced by particle size. We can clearly identify alloying in the catalyst particles, and as electrochemical techniques tend to indicate the absence of Ni from the interface with the electrolyte, the significant gain in activity should be ascribed to influences of the Ni on the active Pt atoms. These are most likely of electronic nature, lowering the electron back-donation to the CO molecules and therefore suppressing the CO adsorption and poisoning on the Pt surface.

4. CONCLUSIONS

PtNi nanocatalysts for methanol oxidation in acid media were prepared on oxygen functionalized carbon nanotubes by microwave assisted polyol reduction using two different modes of irradiation. Nanosized alloy particles well dispersed on the support were obtained. The irradiation mode (either continuous or pulsed) influences both the metal loading and the activity of the prepared catalysts where catalysts prepared under continuous irradiation show higher electrocatalytic activity. Structural characterization confirmed alloy formation, and combined with the electrochemical behavior of the catalysts, an electronic effect has been suggested to discuss the enhancement of activity of the prepared catalysts and their lower CO poisoning compared to benchmark Pt/C E-TEK catalyst and other PtNi catalysts reported in the literature.

■ ASSOCIATED CONTENT

Supporting Information

Temperature profiles during microwave heating, additional TEM images, and additional electrochemical data (CV, mass specific activities, chronoamperometry). This material is available free of charge via the Internet at http://pubs.acs.org

■ AUTHOR INFORMATION

Corresponding Author

*Tel.: +49-345-5525900. Fax: +49-345-5527163. E-mail: michael.bron@chemie.uni-halle.de.

Notes

The authors declare no competing financial interest.

[‖](AB.A.A.N.) On leave from Electronic Materials Research Department, Institute of Advanced Technology and New Materials, City of Scientific Research and Technological Applications (SRTA-City), New Borg Al-Arab City, 21934 Alexandria, Egypt

■ ACKNOWLEDGMENTS

The authors would like to thank Dr. F. Heyroth from the Interdisciplinary Centre of Materials Science at Martin-Luther -University Halle-Wittenberg for performing TEM measurements and E. Koslowski from our institute for performing XRD measurements, which were done at the department of inorganic chemistry of our institute. The central facilities of the department of geology of Martin-Luther-University helped with ICP-OES. AB.A.A.N. gratefully acknowledges a scholarship from the Ministry of Higher Education and Scientific Research (MHESR), Egypt and German Academic Exchange Service (DAAD), Germany, within the program German Egyptian Research Long-Term Scholarship (GERLS) to pursue his Ph.D. studies at Martin Luther University Halle-Wittenberg. We are also grateful to Swiss Light Source, Villigen (Switzerland) for providing beam time and to the staff of SuperXAS beamline for their experimental support.

■ REFERENCES

(1) Dillona, R.; Srinivasana, S.; Aricò, A. S.; Antonucci, V. *J. Power Sources* **2004**, *127*, 112−126.
(2) Kamarudin, S. K.; Achmad, F.; Daud, W. R. W. *Int. J. Hydrogen Energy* **2009**, *34*, 6902−6916.
(3) Arico, A. S.; Srinivasan, S.; Antonucci, V. *Fuel Cells* **2001**, *1*, 133−161.
(4) Aricò, A. S.; Baglio, V.; Antonucci, V. In *Electrocatalysis of Direct Methanol Fuel Cells: From Fundamentals to Applications*; Liu, H., Zhang, J., Eds.; Wiley-VCH: Weinheim, Germany, 2009; pp 1−77.
(5) Huber, G. W.; Iborra, S.; Corma, A. *Chem. Rev.* **2006**, *106*, 4044−4098.
(6) Hamelinck, C. N.; Faaij, A. P. C. *Energy Policy* **2006**, *34*, 3268−3283.
(7) Hamnett, A. *Catal. Today* **1997**, *38*, 445−457.
(8) Wasmus, S.; Küver, A. *J. Electroanal. Chem.* **1999**, *461*, 14−31.
(9) Iwasita, T. *Electrochim. Acta* **2002**, *47*, 3663−3674.
(10) Iwasita, T. In *Handbook of Fuel Cells − Fundamentals, Technology and Applications, Vol. 2: Electrocatalysis*; Vielstich, W., Gasteiger, H. A., Lamm, A., Eds.; John Wiley & Sons: Weinheim, Germany, 2003; pp 603−624.
(11) Antolini, E. In *Electrocatalysis of Direct Methanol Fuel Cells: From Fundamentals to Applications*, Liu, H.; Zhang, J., Eds.; Wiley-VCH: Weinheim, Germany, 2009; pp 227−255.
(12) Iwasita, T.; Hoster, H.; John-Anacker, A.; Lin, W. F.; Vielstich, W. *Langmuir* **2000**, *16*, 522−529.
(13) Choi, J.-H.; Park, K.-W.; Park, I.-S.; Lee, J.-S.; Sung, Y.-E. *J. Electrochem. Soc.* **2006**, *153*, A1812−A1817.
(14) Gasteiger, H. A.; Markovic, N.; Ross, P. N., Jr.; Cairns, E. J. *J. Phys. Chem.* **1993**, *97*, 12020−12029.
(15) Nassr, AB. A. A.; Bron, M. *ChemCatChem* **2013**, *5*, 1472−1480.
(16) Lee, E.; Murthy, A.; Manthiram, A. *J. Electroanal. Chem.* **2011**, *659*, 168−175.
(17) Xu, C.; Hou, J.; Pang, X.; Li, X.; Zhu, M.; Tang, B. *Int. J. Hydrogen Energy* **2012**, *37*, 10489−10498.
(18) Chu, Y.-Y.; Wang, Z.-B.; Jiang, Z.-Z.; Gu, D.-M.; Yin, G.-P. *J. Power Sources* **2012**, *203*, 17−25.
(19) Masud, J.; Alam, M. T.; Awaludin, Z.; El-Deab, M. S.; Okajima, T.; Ohsaka, T. *J. Power Sources* **2012**, *220*, 399−404.

(20) Maiyalagan, T.; Viswanathan, B. *J. Power Sources* **2008**, *175*, 789−793.
(21) Nouralishahi, A.; Khodadadi, A. A.; Rashidi, A. M.; Mortazavi, Y. *J. Colloid Interface Sci.* **2013**, *393*, 291−299.
(22) Justin, P.; Rao, G. R. *Int. J. Hydrogen Energy* **2011**, *36*, 5875−5884.
(23) Hu, C.; Cao, Y.; Yang, L.; Bai, Z.; Guo, Y.; Wang, K.; Xu, P.; Zhou, J. *Appl. Surf. Sci.* **2011**, *257*, 7968−7974.
(24) Gu, D.-M.; Chu, Y.-Y.; Wang, Z.-B.; Jiang, Z.-Z.; Yin, G.-P.; Liu, Y. *Appl. Catal., B* **2011**, *102*, 9−18.
(25) Watanabe, M.; Motoo, S. *J. Electroanal. Chem.* **1975**, *60*, 275−283.
(26) Igarashi, H.; Fujino, T.; Zhu, Y.; Uchida, H.; Watanabe, M. *Phys. Chem. Chem. Phys.* **2001**, *3*, 306−314.
(27) Park, K.-W.; Choi, J.-H.; Kwon, B.-K.; Lee, S.-A.; Sung, Y.-E.; Ha, H.-Y.; Hong, S.-A.; Kim, H.; Wieckowski, A. *J. Phys. Chem. B* **2002**, *106*, 1869−1877.
(28) Harish, S.; Baranton, S.; Coutanceau, C.; Joseph, J. *J. Power Sources* **2012**, *214*, 33−39.
(29) Sakthivel, M.; Schlange, A.; Kunz, U.; Turek, T. *J. Power Sources* **2010**, *195*, 7083−7089.
(30) Das, S.; Mukhopadhyay, A. K.; Datta, S.; Basu, D. *Bull. Mater. Sci.* **2009**, *32*, 1−13.
(31) Whittaker, G. *Sch. Sci. Rev.* **2004**, *8*, 587−94.
(32) Nassr, A. B. A. A.; Sinev, I.; Grünert, W.; Bron, M. *Appl. Catal., B* **2013**, *142*, 849−860.
(33) Klementiev K. V. *VIPER for Windows*; freeware available at: www.cells.es/Beamlines/CLAESS/software/viper.html. Klementev, K. V. *J. Phys. D: Appl. Phys.* **2001**, *34*, 209−217.
(34) Ankudinov, A. L.; Ravel, B.; Rehr, J. J.; Conradson, S. D. *Phys. Rev. B* **1998**, *58*, 7565−7576.
(35) Li, D.; Komarneni, S. *J. Am. Ceram. Soc.* **2006**, *89*, 1510−1517.
(36) Deivaraj, T. C.; Chen, W.; Lee, J. Y. *J. Mater. Chem.* **2003**, *13*, 2555−2560.
(37) Carpenter, M. K.; Moylan, T. E.; Kukreja, R. S.; Atwan, M. H.; Tessema, M. M. *J. Am. Chem. Soc.* **2012**, *134*, 8535−8542.
(38) Oh, H.-S.; Oh, J.-G.; Kim, H. *J. Power Sources* **2008**, *183*, 600−603.
(39) Shui, J.-L.; Zhang, J.-W.; Li, J. C. M. *J. Mater. Chem.* **2011**, *21*, 6225−6229.
(40) Song, S.; Liu, J.; Shi, J.; Liu, H.; Maragou, V.; Wang, Y.; Tsiakaras, P. *Appl. Catal., B* **2011**, *103*, 287−293.
(41) Lidstrom, P.; Tierney, J.; Wathey, B. *Tetrahedron* **2001**, *57*, 9225−9283.
(42) Gabriel, C.; Halstead, B. S. J.; Mingos, D. M. P. *Chem. Soc. Rev.* **1998**, *27*, 213−223.
(43) Bilecka, I.; Niederberger, M. *Nanoscale* **2010**, *2*, 1358−1374.
(44) Ribeiro, V. A.; Correa, O. V.; Neto, A. O.; Linardi, M.; Spinace, E. V. *Appl. Catal., A* **2010**, *372*, 162−166.
(45) Oh, H.-S.; Oh, J.-G.; Hong, Y.-G.; Kim, H. *Electrochim. Acta* **2007**, *52*, 7278−2785.
(46) Luo, B.; Xu, S.; Yan, X.; Xue, Q. *Electrochem. Commun.* **2012**, *23*, 72−75.
(47) Zhou, X.-W.; Zhang, R.-H.; Zhou, Z.-Y.; Sun, S.-G. *J. Power Sources* **2011**, *196*, 5844−5848.
(48) Kim, H. J.; Choi, S. M.; Nam, S. H.; Seo, M. H.; Kim, W. B. *Catal. Toady* **2009**, *146*, 9−14.
(49) Yuan, C.; Zhang, X.; Su, L.; Gao, B.; Shen, L. *J. Mater. Chem.* **2009**, *19*, 5772−5777.
(50) Parreira, L. S.; Martins da Silva, J. C.; D'Villa -Silva, M.; Simões, F. C.; Garcia, S.; Gaubeur, I.; Cordeiro, M. A. L.; Leite, E. R.; Coelho dos Santos, M. *Electrochim. Acta* **2013**, *96*, 243−252.
(51) Johansson, G.; Hedman, J.; Berndtsson, A.; Klasson, M.; Nilsson, R. *J. Electron Spectrosc. Relat. Phenom.* **1973**, *2*, 295−317.
(52) Cameron, S. D.; Dwyer, D. J. *Surf. Sci.* **1986**, *176*, L857−L862.
(53) Manson, M. G. *Phys. Rev. B* **1983**, *27*, 748−762.
(54) Wertheim, G. K.; Dicenzo, S. B.; Youngquist, S. E. *Phys. Rev. Lett.* **1983**, *51*, 2310−2313.
(55) Loukrakpam, R.; Luo, J.; He, T.; Chen, Y.; Xu, Z.; Njoki, P. N.; Wanjala, B. N.; Fang, B.; Mott, D.; Yin, J.; Klar, J.; Powell, B.; Zhong, C.-J. *J. Phys. Chem. C* **2011**, *115*, 1682−1694.
(56) Hwang, B.-J.; Sarma, L. S.; Chen, J.-M.; Chen, C.-H.; Shih, S.-C.; Wnag, G.-R.; Liu, D.-G.; Lee, J.-F.; Tang, M.-T. *J. Am. Chem. Soc.* **2005**, *127*, 11140−11145.
(57) Cui, C.; Ahmadi, M.; Behafarid, F.; Gan, L.; Neumann, M.; Heggen, M.; Cuenya, B. R.; Strasser, P. *Faraday Discuss.* **2013**, *162*, 91−112.
(58) Wang, C.; Chi, M.; Li, D.; Strmcnik, D.; van der Vliet, D.; Wang, G.; Komanicky, V.; Chang, K.-C.; Paulikas, A. P.; Tripkovic, D.; Pearson, J.; More, K. L.; Markovic, N. M.; Stamenkovic, V. R. *J. Am. Chem. Soc.* **2011**, *133*, 14396−14403.
(59) Yu, X.; Wang, D.; Peng, Q.; Li, Y. *Chem.—Eur. J.* **2013**, *19*, 233−239 +.
(60) Sharma, S.; Ganguly, A.; Papakonstantinou, P.; Miao, X.; Li, M.; Hutchison, J. L.; Delichatsios, M.; Ukleja, S. *J. Phys. Chem. C* **2010**, *114*, 19459−19466.
(61) Arenz, M.; Mayrhofer, K. J. J.; Stamenkovic, V.; Blizanac, B. B.; Tomoyuki, T.; Ross, P. N.; Markovic, N. M. *J. Am. Chem. Soc.* **2005**, *127*, 6819−6829.
(62) Luo, B.; Xu, S.; Yan, X.; Xue, Q. *J. Electrochem. Soc.* **2013**, *160*, F262−F268.